2021 IEEE/RSJ International Conference on Intelligent Robots and Systems (IROS)
September 27 - October 1, 2021. Prague, Czech Republic

2021 IEEE/RSJ International Conference on Intelligent Robots and Systems (IROS) | 978-1-6654-1714-3/21/$31.00 ©2021 IEEE | DOI: 10.1109/IROS51168.2021.9635861

Geometric Motion Planning for a System on the Cylindrical Surface

Shuoqi Chen[1], Ruijie Fu[1], Ross Hatton[2] and Howie Choset[1]

***Abstract*— Traditional geometric mechanics models used in locomotion analysis rely heavily on systems having symmetry in $SE(2)$ (i.e., the dynamics and constraints are invariant with respect to a system's position and orientation) to simplify motion planning. As a result, the symmetry assumption prevents locomotion analysis on non-flat surfaces because the system dynamics may vary as a function of position and orientation. In this paper, we develop geometric motion planning strategies for a mobile system moving on a position space whose manifold structure is a cylinder: constant non-zero curvature in one dimension and zero curvature in another. To handle this non-flat position space, we adapt conventional geometric mechanics tools - in particular the system connection and the constraint curvature function - to depend on the system orientation. In addition, we introduce a novel constraint projection method to a variational gait optimizer and demonstrate how to design gaits that allow the example system to move on the cylinder with optimal efficiency.**

I. INTRODUCTION

Self-powered locomotion, in which systems coordinate their internal degrees of freedom to move through a complex environment, is an important capability for both living organisms and robots [1]. To study this, geometric mechanics has been widely applied to develop effective motion plans for locomoting systems [2]. The geometric mechanics framework divides a system's configuration space into two constituent spaces: a position space and a shape space. The position space locates the system, and the shape space corresponds to the system's internal shape (such as its joint angles). Our on-going research, along with many others [3]-[11], seeks to create a rigorous formulation for those systems to move through a series of self-deformations.

Often, one must look at a simpler system to gain an initial understanding of the fundamental principles. A common locomotion model is the so-called three-link mobile robots [12] [13], because its mathematical formulation is tractable and yet elucidates many challenges common to more complicated multi-link systems. Much of the mathematical elegance of the three-link robots arises from their inherent symmetry, which corresponds to the specification that the system's dynamics and constraints are invariant to changes in the system's position and orientation [6][7][12]. Other than a few exceptions in [9] and [10], most existing studies of three-link locomoting systems avoided symmetry-breaking problems and limited their analyses to planar surfaces.

*This work was not supported by any organization

[1]Shuoqi Chen, Ruijie Fu, and Howie Choset are with the Robotics Institute at Carnegie Mellon University, Pittsburgh, PA 15213, USA. shuoqic,ruijief,choset@andrew.cmu.edu

[2]Ross Hatton is with the School of Mechanical, Industrial, and Manufacturing Engineering at Oregon State University, Corvallis, OR 97331, USA. hattonr@oregonstate.edu

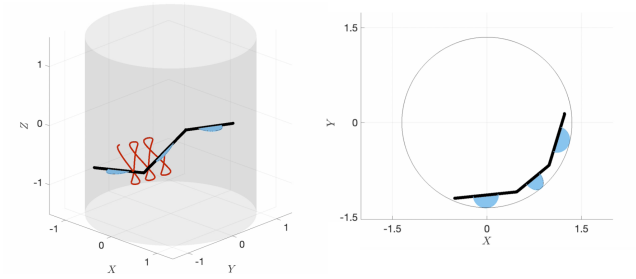

Fig. 1. Isometric view (left) and top view (right) of the quasi-static system on cylinder moving on a inner cylindrical surface using the optimal efficiency gait.

In this paper, we are interested in systems locomoting on non-flat terrains, which violates the symmetry assumption. To this end, we study a novel three-link model called the system-on-cylinder. This new model allows us to explore to what extent the conventional geometric concepts, such as the local connection and the Lie bracket techniques, can be used in motion planning on a curved position space [14].

Using this three-link model, we show that a rotational asymmetry arises when the system's mechanical constraints vary over the position space, and that the overall system motion over a gait depends on the initial orientation of the system body. Furthermore, we present a gait optimization strategy adapted from [17]-[19] that addresses the rotational asymmetry of the system-on-cylinder.

II. BACKGROUND

Our work is based on a series of developments in geometric mechanics community, including [2]-[17]. In this section, we review several key concepts and notations in the framework of geometric mechanics that our paper will closely follow.

A. Geometric Locomotion Model

For a three-link system, the configuration space Q naturally decomposes into a position space G and a shape space M, such that the position $g \in G$ locates the system in the world frame, and the shape $r \in M$ tells the relative arrangements of each component of the system. For systems with first-order dynamics, there exists a linear relationship (which itself is a function of shape) between changes in the system's shape and changes in its position

$$\mathring{g} = -\boldsymbol{A}(r)\dot{r}, \tag{1}$$

in which $\mathring{g}$ represents the system body frame velocities, and $\dot{r}$ represents the shape velocities. Equation (1) is called the

kinematic reconstruction equation, in which the matrix $\boldsymbol{A}(r)$ is the local connection and acts as a Jacobian-like matrix linking the shape velocities and the position velocities [2]. Each row of $-\boldsymbol{A}(r)$ relates one position component with respect to all of the system shape components.

B. Gaits

A gait is a cycle Ω in the shape space that produces a displacement g_Ω in the position space. One line of effort to find good gait designs [13]-[14] focuses on measuring how "non-canceling" the system dynamics are over periodic shape changes. The core principle is that the net displacement g_Ω of a gait can be approximated – although the accuracy of the approximation depends on the choice of the system body frame – by a surface integral of the constraint curvature $D(-\boldsymbol{A})$ of the local connection [14]

$$g_\Omega = \oint_\Omega -g\boldsymbol{A} \approx \iint_{\Omega_a} D(-\boldsymbol{A}). \tag{2}$$

The right side of (2) is formally known as the corrected body velocity integral (cBVI) [14]. The core contribution in this line of work is to recognize the approximated displacement induced by a gait depends only on the gait's path in the shape space. In (2), $D(-\boldsymbol{A})$ captures both how changes in $\boldsymbol{A}$ across the shape space prevent the net-induced motions from cancelling out over a cycle, and how translations and rotations in the induced motions couple into "parallel parking" effects that contribute to the net displacement.

C. Identifying Optimal Gaits

When evaluating the design and performance of three-link robots, we care about finding the best gaits that achieve specific objectives, such as yielding the maximum displacement g_Ω or moving with optimal efficiency $\frac{g_\Omega}{s}$ (efficiency is defined as the gait displacement divided by the gait execution cost s)[1]. Although several gait design strategies exist in [19]-[20], in this paper we focus on using the variational gait optimizer introduced in [17]. This gait optimizer has several advantages. First, it encodes geometric mechanics insights into a fast and theoretically-sound variational algorithm. Second, the optimizer automatically converges to locally optimal results while providing easy ways to specify different cost functions.

The variational gait optimizer uses a gradient-descent based solver to facilitate optimization. For example, to find the optimal efficiency gait, the optimizer searches for gaits along the gradient of efficiency $\frac{g_\Omega}{s}$ with respect to the gait parameterization p until the gradient goes to zero [17]

$$\nabla_p \frac{g_\Omega}{s} = \frac{1}{s}\nabla_p g_\Omega - \frac{g_\Omega}{s^2}\nabla_p s. \tag{3}$$

[1]The gait displacement g_Ω can be calculated using (2), and the gait efficiency $\frac{g_\Omega}{s}$ can be calculated under different system assumptions as specified in [17] and [18]. In our study, we use the weighted pathlength cost in [19] for drag-dominated systems.

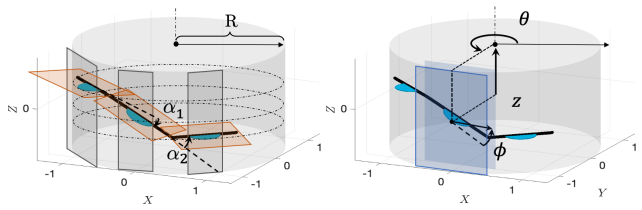

Fig. 2. (Left) the shape variables α_1 and α_2 are the control joint angles of the system-on-cylinder. (Right) the position variable θ is the angular coordinate of a cylindrical system, whose origin is located at some point along the cylinder centerline. z is the vertical distance between the cylinder contact point and the origin of the cylindrical system. ϕ is the orientation of the link in 3D projected onto local tangent plane (shaded blue).

After factoring out a common coefficient of $\frac{1}{s}$, the first part of the gradient $\nabla_p g_\Omega$ contributes towards the displacement maximization

$$\nabla_p g_\Omega \approx \nabla_p \iint_{\Omega_a} D(-\boldsymbol{A}) = \oint_\Omega (\nabla_{p_\perp}\Omega) \lrcorner (D(-\boldsymbol{A})), \tag{4}$$

where the net displacement is approximated by the area integral of $D(-\boldsymbol{A})$, which is then transformed into the interior product of boundary gradient and integrand using the Leibniz's rule [21]. Similarity, $\nabla_p s$ in the second part of the gradient constrains the growth of the gait trajectory by measuring how variations in the gait affect the cost of executing it.

III. Mechanical Model of the System on Cylinder

To study how non-flat surfaces break the symmetry of three-link systems and subsequently affect their motion, we start with a simple model designed to constrain its locomotion to a cylindrical surface. In this section, we first describe the mechanical structure of this model we call the system-on-cylinder, and then we investigate what geometric mechanics tools can be used to analyze the system's locomotion.

A. System Setup

The system-on-cylinder consists of three rigid links with semi-circular "friction" pads located at the link centers. The friction pads are assumed to be in contact with the inner wall of the cylinder at all time as if the pads were magnetic and the cylinder metal. Each pad provides linear drag forces with respect to the velocities along and perpendicular to the corresponding link, and a linear torque with respect to the link's angular velocity. For simplicity, we assume gravity has no effect on the friction model. We specify the links in the system to be connected by 3D joints. Each 3D joint has full yaw (α), pitch (β) and roll (γ) degrees of freedom as shown in Fig.3.

Using the cylindrical coordinates, each contact point between the friction pad and the cylindrical surface defines a local tangent plane with the coordinates $[\theta,\ z]$ as shown in Fig.2. Furthermore, we specify the orientation of the link using the angle ϕ between the link itself and the cross-section

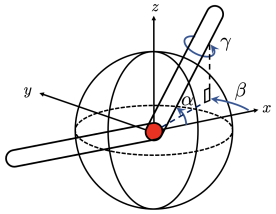

Fig. 3. An example drawing of the 3D joint connecting the links of the system-on-cylinder. The joint angles α, β, and γ move in tandem. Given a particular system orientation ϕ and the control angles α, the compliant angles β and γ can determined accordingly.

of the cylinder, projected onto the local tangent plane. For a cylindrical surface with a constant radius R, the position and orientation of each link i can be uniquely defined by the set of position variables $[\theta_i,\ z_i,\ \phi_i]$ in Fig.2. For the rest of the paper, we will use the middle-link position space variables to represent the system positions θ, z and orientation ϕ.

To succinctly describe the system configurations, we impose two important mechanical constraints:

1) Each friction pad has one and only one contact point with the inner cylindrical surface, and the pads are perpendicular to the local tangent planes of the cylinder wall at the contact points.
2) Both ends of the middle link have the same distance to the cylinder center line, so that middle link is parallel to the local tangent plane.

With constraint 1), the 3D joints can be controlled by the three rotational joint angles α, β, and γ in sequence and form a unique system shape. Adding in constraint 2), we ensure that when one of the three angles of a 3D joint is controlled, the other two can be uniquely determined by functions of the control angles and the system orientation ϕ. We choose the two yaw angles $[\alpha_1,\ \alpha_2]$ as the shape variables and they dictate the links' relative positions with respect to each other. Subsequently, the pitch and roll angle pairs (β and γ) become compliant. The relationship between the joint angles α, β, γ and the orientation variable ϕ are purely geometric, and it can be described by the following equations [2]

$$(2(R-d)+l\sin\beta)^2 + l^2(\cos\phi+\cdots \\ \cos\beta\cos(\alpha-\phi))^2 - 4(R-d)^2 = 0, \tag{5}$$

and

$$l(\sin(\phi_o+\alpha)\cos\gamma - \cos(\alpha+\phi)\sin\beta\sin\gamma)(\cos\phi+\cdots \\ cos(\phi+\alpha)\cos\beta) + \cos\beta\sin\gamma(2d-2R+l\sin\beta) = 0, \tag{6}$$

[2]The control and compliant angle relationships in (5) and (6) are purely geometric, established by both the two mechanical constraints imposed on the system configuration and the curvature of the cylindrical surface. The two equations calculate the β and γ angles for the distal link (i.e. link $i+1$) in the system but can be adapted for the proximal link (i.e. link $i-1$) with appropriate sign changes.

where R is the cylinder radius, l is the link length, and d is the friction pad height. The equations provided above are for the system moving on the inward surface of the cylinder, but they can be generalized to the system moving on the outward cylindrical surface with a few sign switches.

The complexity of (5) and (6) makes it hard to obtain analytical solutions whenever β and γ are involved. For this reason, we represent many of the variables as the sum of partial derivatives and solve them numerically.

B. Orientation-Dependent Local Connection

When establishing the mechanical setup of the system-on-cylinder, we assume that the drag forces induced by the friction pads dominate the dynamics, and inertial effects are immediately damped out. This allows us to make the system-on-cylinder a quasi-static model and reduce the second-order dynamics down to the first-order. At each link, the drag force is linearly related to directional velocity

$$\begin{bmatrix} F_x \\ F_y \\ \tau \end{bmatrix} = \begin{bmatrix} c_x & 0 & 0 \\ 0 & c_y & 0 \\ 0 & 0 & c_\theta \end{bmatrix} \begin{bmatrix} \mathring{g}_x \\ \mathring{g}_y \\ \mathring{g}_\theta \end{bmatrix}, \tag{7}$$

in which $\mathring{g}_i$ is the body velocity of each link, c_x, c_y are the drag coefficients along and perpendicular to the link, and c_θ is the rotational drag coefficient. Given that the total force on a quasi-static system should equal to zero, we can transform the force on each link to the center link frame and yield this following equation

$$\underbrace{\left(\sum_{i=3} J_i^\top c\ J_i\right)}_{M} \begin{bmatrix} \mathring{g} \\ \dot{r} \end{bmatrix} = 0, \tag{8}$$

where c is the diagonal drag matrix in (7), and $J_i = T_g L_{g_i}^{-1} (J_i^w) \widetilde{T_e L_g}$ maps between the body velocity of the system and the body velocity of local link i. The 3×5 M matrix is called the system full Jacobian matrix.

The inverse left lifted action

$$T_g {L_g}_i^{-1} = \begin{bmatrix} \cos(\phi_i) & \sin(\phi_i) & 0 \\ -\sin(\phi_i) & \cos(\phi_i) & 0 \\ 0 & 0 & 1 \end{bmatrix} \tag{9}$$

rotates the world velocity of each link to the link's frame, and

$$\widetilde{(T_e L_g)} = \begin{bmatrix} \cos(\phi) & -\sin(\phi) & 0 & 0 & 0 \\ \sin(\phi) & \cos(\phi) & 0 & 0 & 0 \\ 0 & 0 & 1 & 0 & 0 \\ 0 & 0 & 0 & 1 & 0 \\ 0 & 0 & 0 & 0 & 1 \end{bmatrix} \tag{10}$$

maps from the system body velocity to the system world velocity. J_i^w is the Jacobian that maps between the world velocity of the system and that of each link, and can be calculated as

$$J_i^w = \begin{bmatrix} 1 & 0 & \frac{\partial R\theta_i}{\partial \phi} & \frac{\partial R\theta_i}{\partial \alpha_1} & \frac{\partial R\theta_i}{\partial \alpha_2} \\ 0 & 1 & \frac{\partial z_i}{\partial \phi} & \frac{\partial z_i}{\partial \alpha_1} & \frac{\partial z_i}{\partial \alpha_2} \\ 0 & 0 & \frac{\partial \phi_i}{\partial \phi} & \frac{\partial \phi_i}{\partial \alpha_1} & \frac{\partial \phi_i}{\partial \alpha_2} \end{bmatrix}. \tag{11}$$

Taking the left three columns of the system full Jacobian M to be the matrix w_1 and the right two columns to be w_2, we can calculate the body velocity by

$$\mathring{g} = -w_1^{-1} w_2 \dot{r} = -\boldsymbol{A}_{b(g,r)} \dot{r}. \tag{12}$$

Equation (12) is the reconstruction equation for the quasi-static system on cylinder.

In the following sections, we drop the subscripts so that $\boldsymbol{A}_{b(g,r)}$ becomes $\boldsymbol{A}$. It is clear that from the derivation above, the connection $\boldsymbol{A}$ acquires an extra dependency on the system orientation ϕ. Fig.4 visualizes this orientation dependency by portraying the vector field formed by the first row of $\boldsymbol{A}$ that varies with respect to different ϕ values. The effect of ϕ comes from the expression of the system full Jacobian M, and therefore it implicitly reflects how curvature changes in different directions of the cylinder surface affect instantaneous system motion.

C. Orientation-Dependent Constraint Curvature Function

The orientation-dependent connection $\boldsymbol{A}$ also affects how the net displacement over a gait g_Ω is approximated using the Lie bracket averaging techniques, such as the corrected body velocity integral (cBVI). This is because the cBVI is the area integral of the curvature of the connection $\boldsymbol{A}$ as shown in (2); when values of $\boldsymbol{A}$ change with the system orientation, so will the system's cBVI. We recognize the cBVI as an important aid to search for a system's effective gait cycle, so in this section we examine how system orientations can be accounted for in the cBVI to correctly approximate the gait displacement for the system-on-cylinder.

For small amplitude gaits in the shape space of the system, the resulting motion can be captured by the use of Lie brackets. With a specified input shape velocity $\dot{r}$, the system-on-cylinder at configuration $q = (r,\ g)$ has position velocity $\dot{g} = T_e L_g \boldsymbol{A}\ \dot{r}$ within the local tangent plane shown in Fig.3 [3]. Moving with velocity $\dot{r} = [\dot{\alpha_1}, \dot{\alpha_2}]$ can be interpreted as flowing along the vector field $X(q)$ defined over the full configuration space [14]

$$X(q) = \ \dot{q} = \begin{bmatrix} \dot{r} \\ \dot{g} \end{bmatrix} \tag{13}$$

If we define two unit-magnitude input shape velocities

$$\dot{r_1} = [1,\ 0]^\top \text{ and } \dot{r_2} = [0,\ 1]^\top,$$

then the following Lie bracket gives the average velocity vector achieved by infinitesimally flowing along the vector fields, evaluated at the initial configuration $q_0 = (r_0,\ g_0)$ in the system world frame

[3]The term $T_e L_g$ is the lifted action that maps the system's body velocity to its position space spatial velocity [14]

$$[\dot{q}_1, \dot{q}_2] = \left[\begin{pmatrix} \dot{r}_1 \\ \dot{g}_1 \end{pmatrix}, \begin{pmatrix} \dot{r}_2 \\ \dot{g}_2 \end{pmatrix} \right] \tag{14}$$

$$= \begin{bmatrix} \left(\frac{\partial \dot{r}_2}{\partial r}\dot{r}_1 - \frac{\partial \dot{r}_1}{\partial r}\dot{r}_2\right) & + & \left(\frac{\partial \dot{r}_2}{\partial g}\dot{g}_1 - \frac{\partial \dot{r}_1}{\partial g}\dot{g}_2\right) \\ \left(\frac{\partial \dot{g}_2}{\partial r}\dot{r}_1 - \frac{\partial \dot{g}_1}{\partial r}\dot{r}_2\right) & + & \left(\frac{\partial \dot{g}_2}{\partial g}\dot{g}_1 - \frac{\partial \dot{g}_1}{\partial g}\dot{g}_2\right) \end{bmatrix} \Big|_{\substack{r_0 \\ g_0}}. \tag{15}$$

Taking $g_0 = \boldsymbol{e}$ (placing the origin at the initial position of the system) eliminates the lifted action terms [14]. Upon simplification, the bottom three rows of the total Lie bracket in (15) can be separated out into three major components, and the final form of the total Lie bracket can be represented as

$$[\dot{q}_1, \dot{q}_2]\big|_{q_{\boldsymbol{e}}} = \begin{bmatrix} \vec{\mathbf{0}} \\ \underbrace{-\left(\frac{\partial \boldsymbol{A}_2}{\partial r_1}\big|_{\substack{r_0 \\ \phi_0}} - \frac{\partial \boldsymbol{A}_1}{\partial r_2}\big|_{\substack{r_0 \\ \phi_0}}\right)}_{-d\boldsymbol{A}} \\ + \left(\left(\frac{\partial (T_e L_g)}{\partial g}\big|_{q_0} \boldsymbol{A}_2\big|_{\substack{r_0 \\ \phi_0}}\right) \boldsymbol{A}_1\big|_{\substack{r_0 \\ \phi_0}}\right) \\ \underbrace{-\left(\left(\frac{\partial (T_e L_g)}{\partial g}\big|_{q_0} \boldsymbol{A}_1\big|_{\substack{r_0 \\ \phi_0}}\right) \boldsymbol{A}_2\big|_{\substack{r_0 \\ \phi_0}}\right)}_{[\boldsymbol{A}_1, \boldsymbol{A}_2]} \\ + \left(\frac{\partial \boldsymbol{A}_2}{\partial g}\big|_{\substack{r_0 \\ \phi_0}} \boldsymbol{A}_1\big|_{\substack{r_0 \\ \phi_0}}\right) \\ \underbrace{-\left(\frac{\partial \boldsymbol{A}_1}{\partial g}\big|_{\substack{r_0 \\ \phi_0}} \boldsymbol{A}_2\big|_{\substack{r_0 \\ \phi_0}}\right)}_{\text{rotational asymmetry term}} \end{bmatrix}, \tag{16}$$

where $q_{\boldsymbol{e}}$ is the identity configuration of the system in the world frame, and r_0, ϕ_0 are the initial shape and orientation of the system.

Different than three-link system in $SE(2)$ which only contains the exterior derivative $(-\mathrm{d}\boldsymbol{A})$ and the local Lie bracket $[\boldsymbol{A}_1,\ \boldsymbol{A}_2]$, for the system-on-cylinder a third term shows up due to the orientation-dependent connection $\boldsymbol{A}$. The combinatory effect of the exterior derivative, the local Lie bracket, and the rotational asymmetry term is captured by the notation $D(-\boldsymbol{A})$, which is the curvature of the connection r_0 evaluated at system identity configuration $q_{\boldsymbol{e}}$.

$$D(-\boldsymbol{A}) = -\mathrm{d}\boldsymbol{A} + [\boldsymbol{A}_1,\ \boldsymbol{A}_2] + \text{rotational asymmetry term}. \tag{17}$$

The effects of the exterior derivative and the local Lie bracket have been carefully reviewed in [14] for three-link systems in $SE(2)$ and are not repeated here. However, the rotational asymmetry term is a new appearance; it is caused by the cylinder surface curvature which breaks the system symmetry assumption. Nevertheless, there exists an underlying parallelism between the previously discovered local Lie bracket and the new rotational asymmetry term. Whereas the local Lie bracket neglects the effect of local connection $\boldsymbol{A}$ and explains the Lie bracket non-commutativity induced by $T_e L_g$ (the amount of rotation between the world frame and system body frame), the

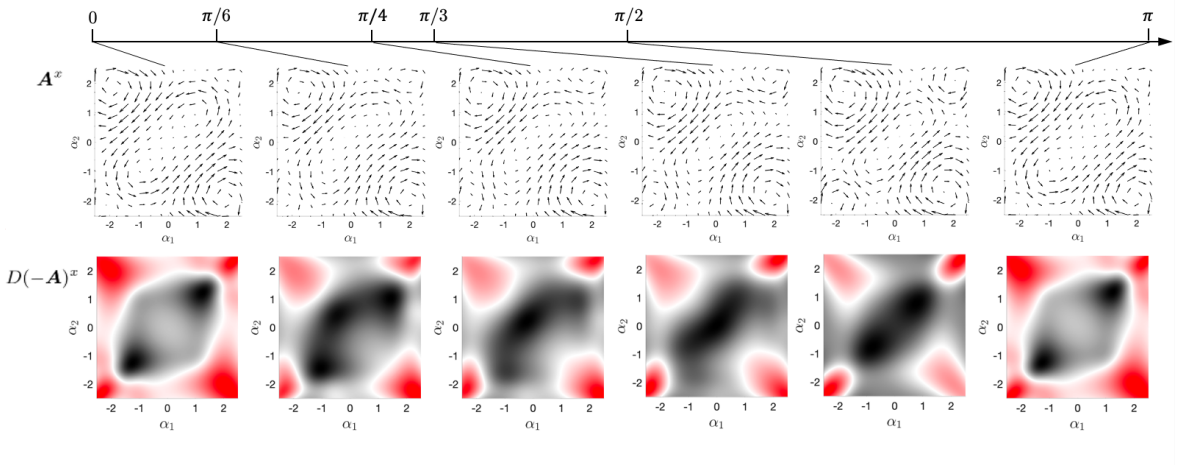

Fig. 4. (Top) the forward-directional connection vector fields (first row of $\boldsymbol{A}$) of the system-on-cylinder when the system is orientated at $\phi_0 = 0, \frac{\pi}{6}, \frac{\pi}{4}, \frac{\pi}{3}, \frac{\pi}{2}$, and π with respect to the world frame. (Bottom) the system constraint curvature function (CCF) in the forward direction (first row of $D(-\boldsymbol{A})$) of the system-on-cylinder at various orientations. The red regions indicate positive CCF values whereas black regions indicate negative CCF values. As ϕ changes, both the connection vector fields and the CCF plots stretch in patterns related to the different surface curvatures at different directions along the cylindrical surface.

rotational asymmetry term neglects the effect of $T_e L_g$ and explains the Lie bracket non-commutativity induced by the different values of $\boldsymbol{A}$ at different position g in the world frame.

IV. Motion Planning Using Constrained Variational Gait Optimization

In section III, we have formulated equations that capture the effect of rotational asymmetry on the system locomotion for the system-on-cylinder. Equation (12) and (17), in particular, establish theoretical foundations to estimate displacement over a gait on the cylindrical surface at different system orientations. In this section, we employ those equations in a motion planning strategy to find the optimal efficiency gait. This optimizer is based on the framework originally presented in [17], which assumed rotation symmetry of the system equations of motion. In this work, we extend the framework to handle the rotational asymmetry by first lifting the shape space of gaits to the shape-and-orientation space, and then restricting variations in the gaits to those that respect the shape-orientation constraints that appear in the local connection.

We have shown in section II that the gradient of the gait efficiency with respect to the gait parametrization can be represented in (3). Among the two differential terms, $\nabla_p s$ is evaluated independent of the change in system orientation ϕ, so we will follow the standard calculus operations in [17]. The calculation of $\nabla_p g_\Omega$, however, uses sign-definite regions of $D(-\boldsymbol{A})$ as shape change attractors and needs to account for the system orientation appropriately. Because $D(-\boldsymbol{A})$ takes different values as a function of different system orientation ϕ, we expand the shape space to include ϕ as its third dimension, and augment the local connection as $\tilde{\boldsymbol{A}} = [\boldsymbol{A_1}\ \boldsymbol{A_2}\ \mathbf{0}]$. The corresponding augmented curvature $D(-\tilde{\boldsymbol{A}})$ contains three components.[4] Using the Leibniz rule [5], (4) can be represented in the generalized form

$$\begin{aligned}\nabla_p \iint_{\Omega_a} D\left(-\tilde{\boldsymbol{A}}\right) &= \oint_{\Omega} (\nabla_p \Omega) \lrcorner D\left(-\tilde{\boldsymbol{A}}\right) \\ &= \oint_{\Omega} \Big[(\nabla_{p_\perp} \Omega) \lrcorner D\left(-\tilde{\boldsymbol{A}}\right)_{\parallel\perp} \\ &\qquad + (\nabla_{p_\circlearrowleft} \Omega) \lrcorner D\left(-\tilde{\boldsymbol{A}}\right)_{\parallel\circlearrowleft} \Big],\end{aligned} \tag{18}$$

in which the local basis $e_\parallel$ is tangent to the current gait trajectory, $e_\perp$ is normal to the gait in its local tangent plane, and $e_\circlearrowleft$ is binormal to the gait [18].

Equation (18) essentially provides the gradient of the net displacement of a 3D gait trajectory if the shape variables are all freely controllable. However, this is not the case for the system-on-cylinder. Movement of any point on the gait Ω along the augmented ϕ dimension is constrained by the point's movement along α_1 and α_2 dimensions following the velocity constraint

$$\dot{\phi} = \boldsymbol{A}^\phi \begin{bmatrix} \dot{\alpha_1} \\ \dot{\alpha_2} \end{bmatrix}, \tag{19}$$

where $\boldsymbol{A}^\phi$ is the third row of the original connection matrix without the shape space augmentation. Calculation of the gait performance gradient should satisfy this relationship.

To respect the velocity constraint, We utilize the fact that constraints imposed on the gradient of the boundary with respect to boundary variations can be equivalently applied to the gradient of an integral with respect to those variations.

[4]For systems with 3D shape space, the exterior derivative, local Lie bracket and rotational asymmetry term in (16) each have three components, corresponding to the available pairs of basis vectors as specified in [19].

[5]The Leibniz rule provides a powerful way to contract $D(-\boldsymbol{A})$ along $\nabla_p g_\Omega$ to produce a differential one-form that can be integrated over the gait Ω [21].

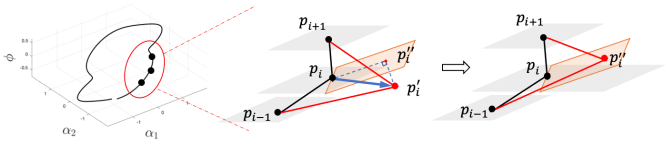

Fig. 5. The process of constraint plane projection. At each waypoint p_i along the gait, the correct movement of p_i in the augmented 3D shape space (left) is along the gait expansion vector (blue arrow; middle) calculated by (18), then projected onto the constraint plane C_i (orange plane; middle and right).

Because we use waypoints p to describe the boundary of a gait, enforcing the velocity constraint on the gait segment adjoining each waypoint p_i ensures that the gradient of the gait also abides by the constraint. To satisfy the constraint at the waypoint level, we construct a constraint plane local to a waypoint p_i, so that moving along α_1 and α_2 in ϕ direction is calculated by (19). A local constraint plane C_i at waypoint p_i is defined by the point $[\alpha_{1i}, \alpha_{2i}, \phi_i]$, and the normal vector $\hat{n}_i$ of the local constraint plane can be formulated as

$$\hat{n}_i = \begin{bmatrix} \Delta r_1 \\ \boldsymbol{A}^{\phi} \cdot \Delta r_1 \end{bmatrix} \times \begin{bmatrix} \Delta r_1 \\ \boldsymbol{A}^{\phi} \cdot \Delta r_2 \end{bmatrix}. \tag{20}$$

where $\Delta r_1 = \dot{r_1}\Delta t = [1, 0]^\top$ and $\Delta r_2 = \dot{r_2}\Delta t = [0, 1]^\top$ are two unit-magnitude inputs in the α_1, α_2 subspace.

The process of finding $\nabla_p g_\Omega$ for an optimal efficiency gait can then be implemented as a two-step process. First, move the trajectory of the gait in a direction such that it maximizes the flux of a vector field corresponding to the augmented $D(-\boldsymbol{A})$,[6] as if all three variables in the 3D shape space are freely controllable. Second, project the gradient vector to the velocity constraint plane at the gait boundary, and then use the projected gradient as the direction to expand or contract the shape of the gait.

V. Discussion

We ran the constrained variational gait opitmization on the system-on-cylinder to find two sets of gait. The first set maximizes the displacement in the forward direction (with the gradient $\nabla_p g_\Omega$), and the second set maximizes the gait operation efficiency (with the gradient specified in (3)). To examine the effect of system orientation on its locomotion, the optimal gaits are generated starting from various starting orientation ϕ_0. Fig.6 and Fig.7 illustrate the stack of gaits under the two performance metrics in the augmented 3D shape space.

Because the gradients of both the maximal displacement gaits and the optimal efficiency gaits include the orientation dependent term $\nabla_p g_\Omega$, the optimal gaits of either set take different shapes and correspondingly different position space trajectories at various values of system orientations ϕ. We observe that maximal displacement gaits generally enclose

[6]The vector field associated with $D(-\boldsymbol{A})$ is formed by associating each local plane in $\mathbb{R}^3$ shape space (i.e. spanned by two out of the three local basis vectors $e_\parallel, e_\perp, e_\circlearrowleft$) with its normal vector. Existence of this vector field is due to the separation of the constraint curvature in to local components in high-dimensional shape space

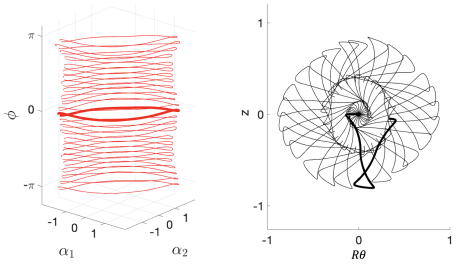

Fig. 6. The maximal displacement gaits (left) and the resulting position space trajectories (right) corresponding to different starting orientation ϕ_0. The bold lines show the optimal displacement gait at $\phi_0 = 0$. See the supplementary video for simulations.

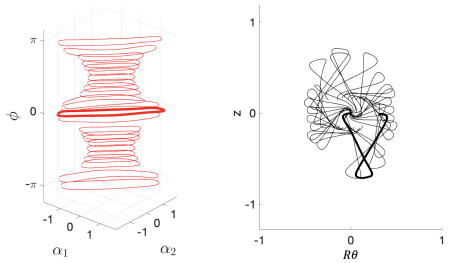

Fig. 7. The optimal efficiency gaits (left) and the resulting position space trajectories (right) corresponding to different starting orientation ϕ_0. The bold lines show the optimal efficiency gait at $\phi_0 = 0$. See the supplementary video for simulations.

as much sign-definite region as possible, while the optimal efficiency gaits tighten up pathlength and sacrifice areas with low absolute values in exchange for lower cost along the gait. The balance between large net displacement over gait and the cost of executing the gait is illustrated in Fig.8. Optimal gaits that start from and evolve around $\phi \in \{-\pi, 0, \pi\}$ appear larger than those of other ϕ values, which correctly relates back to the calculated values of the constraint curvature functions (CCFs), which are the rows of $D(-\boldsymbol{A})$. For the CCF values corresponding to position variable x, sign-definite areas are wider in range and larger in values at $\phi \in \{-\pi, 0, \pi\}$.

One thing to note is that, whereas we required our designed gait to return to the same starting shape (i.e. the control angles α_1 and α_2 resume their original values at the beginning of the gait), we did not specify the same for the system orientation ϕ. As such, it is possible for the system executing the optimal gait to end up at a different orientation than where it starts. Despite this slack we give to our algorithm, we discovered that both the optimal efficiency and the maximal displacement gaits produce very little net rotation. This corresponds to the observation that the optimal gaits and the CCF in the ϕ direction are relatively axial-symmetric around the center of shape space, therefore accumulative system rotation largely cancels itself over each gait cycle.

VI. Conclusions

In this paper, we examined how position space curvature affects the motion of a quasi-static three-link system on a cylindrical surface, specifically through the derivation of the

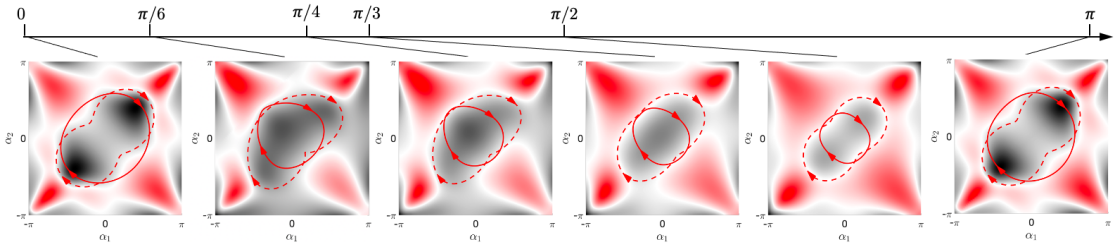

Fig. 8. Superposition of the maximal displacement and the optimal efficient gaits for the system-on-cylinder, starting from initial orientation $\phi_0 = 0, \frac{\pi}{6}, \frac{\pi}{4}, \frac{\pi}{3}, \frac{\pi}{2}$, and π in the world frame. The red dashed lines indicate the maximal displacement gaits, and the red sold lines indicate the optimal efficiency gaits. Bot sets of the gaits are plotted over the fitted CCF planes, which best fit the oriented curve of the optimal efficiency gaits in the augmented 3D shape space. The red shaded regions indicate positive CCF values whereas black regions indicate negative values.

connection $\boldsymbol{A}$ and the constraint curvature function $D(-\boldsymbol{A})$. We showed that the surface curvature of a cylinder breaks the system symmetry by inducing a change in the connection vector fields with respect to the system orientation ϕ. This dependency on orientation propagates to the use of the Lie brackets to approximate large system motion. As a result, we discovered a rotational asymmetry term that appears in $D(-\boldsymbol{A})$ of systems on non-flat surfaces, which encodes information of the position space curvature. In addition, we extended the existing variational gait optimizer by introducing a new constraint projection procedure to our gradient calculation, so that orientation dependency of the system locomotion is carefully preserved during optimization.

As an example of symmetry-breaking systems, the system-on-cylinder paves the way for future motion planning of systems locomoting on a more diverse set of surfaces. Specifically, surfaces that exhibit periodicity are of interest as the cyclical curvature pattern can be leveraged in open-loop gait design. We also plan to expand our work to cover other systems, such as the high Reynolds swimmers or the kinematic snake model in a realistic environment where gravity matters. In a broader scope, we hope to use our findings to develop a motion planning framework for general symmetry-breaking systems. Such framework would ideally explain symmetry-breaking phenomenon induced not only by position space curvature but also by non-conservative external actuation, such as directional forces acting on the locomoting systems.

REFERENCES

[1] Aguilar, Jeffrey, et al. "A review on locomotion robophysics: the study of movement at the intersection of robotics, soft matter and dynamical systems." Reports on Progress in Physics 79.11 (2016): 110001.

[2] Hatton, Ross L., and Howie Choset. "Geometric motion planning: The local connection, Stokes' theorem, and the importance of coordinate choice." The International Journal of Robotics Research 30.8 (2011): 988-1014.

[3] Walsh, Gregory C., and S. Shankar Sastry. "On reorienting linked rigid bodies using internal motions." IEEE Transactions on Robotics and Automation 11.1 (1995): 139-146.

[4] Hatton, Ross L., et al. "Geometric visualization of self-propulsion in a complex medium." Physical review letters 110.7 (2013): 078101.

[5] Avron, Joseph E., and Oren Raz. "A geometric theory of swimming: Purcell's swimmer and its symmetrized cousin." New Journal of Physics 10.6 (2008): 063016.

[6] Melli, Juan B., Clarence W. Rowley, and Dzhelil S. Rufat. "Motion planning for an articulated body in a perfect planar fluid." SIAM Journal on applied dynamical systems 5.4 (2006): 650-669

[7] Ostrowski, James Patrick. The mechanics and control of undulatory robotic locomotion. Diss. California Institute of Technology, 1996.

[8] Kelly, Scott D., and Richard M. Murray. "Geometric phases and robotic locomotion." Journal of Robotic Systems 12.6 (1995): 417-431.

[9] Dear, Tony, et al. "The three-link nonholonomic snake as a hybrid kinodynamic system." 2016 American Control Conference (ACC). IEEE, 2016.

[10] Grover, Jaskaran, et al. "Geometric motion planning for a three-link swimmer in a three-dimensional low Reynolds-number regime." 2018 Annual American Control Conference (ACC). IEEE, 2018.

[11] Gong, Chaohui, et al. "Geometric motion planning for systems with toroidal and cylindrical shape spaces." Dynamic Systems and Control Conference. Vol. 51913. American Society of Mechanical Engineers, 2018

[12] Shammas, Elie A., Howie Choset, and Alfred A. Rizzi. "Geometric motion planning analysis for two classes of underactuated mechanical systems." The International Journal of Robotics Research 26.10 (2007): 1043-1073.

[13] Hatton, Ross L., and Howie Choset. "Connection vector fields for underactuated systems." 2008 2nd IEEE RAS EMBS International Conference on Biomedical Robotics and Biomechatronics. IEEE, 2008.

[14] Hatton, Ross L., and Howie Choset. "Nonconservativity and noncommutativity in locomotion." The European Physical Journal Special Topics 224.17-18 (2015): 3141-3174.

[15] Hatton, Ross L., and Howie Choset. "Kinematic cartography for locomotion at low Reynolds numbers." Proc. Robot. Sci. Syst. VII (2011).

[16] Hatton, Ross L., and Howie Choset. "Connection vector fields and optimized coordinates for swimming systems at low and high Reynolds numbers." Dynamic Systems and Control Conference. Vol. 44175. 2010.

[17] Ramasamy, Suresh, and Ross L. Hatton. "Soap-bubble optimization of gaits." 2016 IEEE 55th Conference on Decision and Control (CDC). IEEE, 2016.

[18] Ramasamy, Suresh, and Ross L. Hatton. "Geometric gait optimization beyond two dimensions." 2017 American Control Conference (ACC). IEEE, 2017.

[19] Ramasamy, Suresh, and Ross L. Hatton. "The Geometry of Optimal Gaits for Drag-Dominated Kinematic Systems." IEEE Transactions on Robotics 35.4 (2019): 1014-1033.

[20] Hatton, Ross L., Faraji, Hossein F., Brock, Zachary et al. Geometric Motion Planning for Inertial Systems (in preparation). In: (2020) (cit. on pp.2).

[21] Flanders, Harley. "Differentiation under the integral sign." The American Mathematical Monthly 80.6 (1973): 615-627.

[22] Kobayashi, Shoshichi, and Katsumi Nomizu. Foundations of differential geometry. Vol. 1. No. 2. New York, London, 1963.